







## Article

# Physicochemical and Sorption Characteristics of Carbon Biochars Based on Lignin and Industrial Waste Magnetic Iron Dust

Mariia Galaburda <sup>1,2</sup> , Alicja Bosacka <sup>1,3,\*</sup> , Dariusz Sternik <sup>1</sup>, Olena Oranska <sup>2</sup> , Mykola Borysenko <sup>2</sup> , Volodymyr Gun'ko <sup>2</sup>  and Anna Derylo-Marczewska <sup>1,\*</sup> 

<sup>1</sup> Faculty of Chemistry, Institute of Chemical Sciences, Maria Curie-Skłodowska University, Maria Curie-Skłodowska Sq. 3, 20-031 Lublin, Poland

<sup>2</sup> Institute of Surface Chemistry, National Academy of Sciences, General Naumov Street 17, 03164 Kyiv, Ukraine

<sup>3</sup> Faculty of Production Engineering, University of Life Sciences, Gleboka Street 28, 20-612 Lublin, Poland

\* Correspondence: alicja.bosacka@up.lublin.pl (A.B.); anna.derylo-marczewska@mail.umcs.pl (A.D.-M.)

**Abstract:** Magnetosensitive biochars were prepared with mechanochemical ball-milling of lignin and blast furnace dust with further pyrolysis at 800 °C under an inert gas atmosphere. The physicochemical and sorption characteristics of the materials were analyzed using several techniques: low-temperature nitrogen adsorption–desorption, X-ray powder diffraction, Raman spectroscopy, elemental analysis, potentiometric titration, and thermal analysis. All the synthesized biocarbons were characterized by their specific surface areas ( $S_{BET}$ ) in the range of 290–330 m<sup>2</sup>/g and microporous structures with certain contribution of mesopores in the total porosity. Equilibrium adsorption studies revealed the potential applicability of the materials in water remediation from hazardous organic substances modelled with methylene blue (MB) dye. Generally, this study illustrates the effective conversion of sustainable waste into a functional carbon material.

**Keywords:** metallurgical dust; lignin; magnetosensitive biochars; carbons; mechanochemical activation



**Citation:** Galaburda, M.; Bosacka, A.; Sternik, D.; Oranska, O.; Borysenko, M.; Gun'ko, V.; Derylo-Marczewska, A. Physicochemical and Sorption Characteristics of Carbon Biochars Based on Lignin and Industrial Waste Magnetic Iron Dust. *Water* **2023**, *15*, 189. <https://doi.org/10.3390/w15010189>

Academic Editors: Konstantinos Simeonidis and Kiriaki Kalaitzidou

Received: 30 November 2022

Revised: 21 December 2022

Accepted: 29 December 2022

Published: 2 January 2023



**Copyright:** © 2023 by the authors. Licensee MDPI, Basel, Switzerland. This article is an open access article distributed under the terms and conditions of the Creative Commons Attribution (CC BY) license (<https://creativecommons.org/licenses/by/4.0/>).

## 1. Introduction

Dyes and pigments are applied in various industries; for example, printing, leather tanning, the production of textiles, paper, rubber, food, cosmetics, etc. Unfortunately, colored substances strongly and negatively affect the quality of water. The coloration of water can occur even with very low dye concentration. Moreover, numerous dyes, mainly of synthetic origin, are considered hazardous substances for aquatic life, animals, and people and are hard to decompose in water. Therefore, the removal of these substances from water and wastewater is of great importance. Adsorption is one of the most frequently used methods for the removal of organic substances because of its simplicity, high efficiency, high variety of available adsorbents, and low ability to produce pollutants [1,2].

On the material market, a wide range of adsorbents (e.g., silicas, zeolites, carbons, polymers, clays, etc.) are available, but these materials may have some restrictions [3–5]. Novel materials with improved properties that are characterized by high adsorption efficiency, thermal stability, longevity, selectivity, resistance to microbes, and relatively inexpensive production are the subject of this research. Adsorption efficiency depends on some key factors caused by types of adsorbates, adsorbents, and solvents. The adsorption process depends on the structure and size of adsorbate molecules, the presence of various functional groups, adsorbate solubility, dissociation ability, adsorbent surface and structural characteristics (e.g., porous structure, surface chemistry, and ash content), and solution properties (e.g., solvent type, pH, and ionic strength) [1,2,6–8]. Functional groups that are present on the adsorbent surface can play a key role in the interactions between adsorbent and adsorbate. For carbons, the basic or acidic surface sites affect the charge, hydrophobicity, and electric density of carbon layers. Based on the aforementioned factors, which may affect the adsorption efficiency of carbon materials, different absorption mechanisms occur,

including dispersion, hydrogen bonding, donor–acceptor interactions, or competitive water adsorption [7,8].

Biochar-based materials with strictly defined surface properties and characteristics have reached scientists' attention because of their high adsorption efficiency of organic pollutants (e.g., dyes) and environmental friendliness due to their reuse of organic wastes [1]. In this work, biochars based on lignin and industrial iron dust blends were prepared using pyrolysis at a high temperature under restricted oxygen conditions. Pyrolysis and activation are crucial stages in the formation of the texture and structure of biochars that affect adsorption effectiveness. Generally, pyrolysis of selected blends enables the preparation of materials with unique textural, structural, thermal, and adsorption characteristics [9].

Lignin was chosen as a carbon source for several reasons. Firstly, it was chosen due to its prevalence and availability. Lignin is the second most abundant natural amorphous polymer after cellulose [10]. A huge amount of technical lignin is produced every day all over the world. Lignin is commonly viewed as a useless and low-cost industrial solid waste separated from the biomass feedstocks of papermaking industries, such as wood and grass. Secondly, it was chosen because of its aromatic molecular structure. Lignin is a complex biopolymer composed of different amounts of three monolignols, including *p*-coumaryl alcohol, coniferyl alcohol, and sinapyl alcohol [11]. Compared with other bioresources, it consists of a large number of aromatic benzene rings and possesses the highest carbon content of up to 60%, which favours the highly efficient production of biochar. However, due to the complex structure, low chemical reactivity, and presence of organic and inorganic impurities, its further applications are limited, and currently, most lignin is burned for energy. Hence, it can be an optimal choice to use as the feedstock of biochar.

In recent years, researchers have paid great attention to the production of biochars from lignocellulosic biomass to reduce the cost of biomass utilization [12,13]. Different methods for the preparation of carbon sorbents from lignin were reviewed, such as pyrolysis at high temperatures, steam activation, or chemical activation aiming to increase biochar porosity or structure. Chatterjee described [14] that the content of lignin controlled the char yield and consequently controlled the activated carbon yield. Thus, the type of lignin as well as the microstructure of the char yield depend on the source of biomass and the amount of cellulose and lignin. Lignin-derived biochar is a promising, sustainable alternative to petroleum-based carbon powders (e.g., carbon black) for polymer composite and energy storage applications for high-performance capacitors [15,16]. Demir M. and co-authors reported the economic and sustainable syntheses of functional lignin-derived carbons for supercapacitor and CO<sub>2</sub> capture applications [17]. In another work, Demir M. successfully obtained graphitic carbon via the hydrothermal carbonization and catalytic graphitization of biochar using nitrates Fe(II), Co(II), or Mn(II) as catalysts at 900–1100 °C [18]. Zijun Yi et al. investigated the impact of different pyrolysis atmospheres on the properties of lignin-derived biochar and determined that CO<sub>2</sub> accelerated the removal of the aliphatic structures and rendered the biochar of hydrophobic surface, but formed less fragmented structures than that obtained in N<sub>2</sub> [19]. Thus, the potential of biochar and lignin-based adsorbents for wastewater treatment (to remove dyes, antibiotics, organics, and heavy metals) has received particular attention in recent years [20–24].

Different methods of modifications that changed the adsorption, catalytic, and magnetic properties of biochar were mainly conducted by mixing metal oxides, metal salts, carbonaceous materials, and biochars [25]. The magnetic properties of biochars are usually enhanced by iron salt or iron metal oxide. To the best of our knowledge, no report on lignin-derived biochars filled with magnetic metallurgical dust exists. That is why such a possibility is considered in this work.

According to the World Steel Association, world crude steel production in 64 countries was 143.3 million tons in November 2021 [26]. Ukraine was in 14th place on the list of “Major steel-producing countries 2021 and 2020” with 21.4 million tons of crude steel production as well as 21.2 million tons of pig iron.

The main product of blast furnace production is cast iron, and by-products include slag and blast furnace gas. Smelting products released from the furnace are sent for processing, including cast iron that is processed for pouring into ingots on a filling machine, slag that is processed for granulation, and blast furnace gas that is processed for purification [27]. Blast furnace production is considered to be the most ecologically dirty link of the technological cycle as it generates 60–65% of wastes. Gravity dust collectors, cyclone dust collectors, bag dust collectors, and other devices are used to obtain flue dust. The sludge is recycled as a waste product after wet cleaning of blast furnace gas. It is used for the blast furnace charge due to its high content of iron oxides. These solid wastes contain many valuable products that can be reused. They usually contain zinc, iron, carbon, and other ferrous and non-ferrous metals and are classified as a secondary resource of zinc and iron. The chemical composition of dust varies to a large extent. Dust from a furnace under high pressure contains 14.6 SiO<sub>2</sub>, 4.35 MgO, 4.35 Al<sub>2</sub>O<sub>3</sub>, 11.85 CaO, 0.74 S, and 3.75 MnO wt.%, and the rest is iron oxides. From a technological point of view, the sludge is very difficult to process due to the high content of non-ferrous metals. By separating particles into fine and coarse fractions, 50–60% of zinc and lead can be removed, and 80% of the total annual volume of generated sludge can be recycled. The particle size of blast furnace dust is about 5–120 µm. The composition of the sludge includes heavy non-ferrous metals—mainly zinc, lead, fluids, chlorides, and sulphates. They have a good flow ability and cause secondary pollution which can be suspended in the air for a long time [28]. Many steel plants around the world have already taken innovative measures to recycle 100% of these wastes with the ultimate goal of improving the efficiency of the steel industry. Blast furnace slags in some countries do not even have the status of waste but belong to secondary raw materials due to effective use as raw materials in several areas (e.g., road construction, the production of cement and concrete in the form of crushed stone, and mixtures without binders or with binders) [29–32]. However, it remains relevant for Ukraine [33].

The disposal of technological waste is a complex resource and environmental problem. The recovery and reuse of this solid waste in an enterprise or industrial facility is mainly necessary to protect the environment and conserve metals and minerals. Studies on improving waste processing technologies and the disposal of metallurgical slags, including dust, are of considerable interest. The problem of organizing zero-waste technology using waste from adjacent industries, the return of waste, shavings, and other dispersed metal waste to metal circulation, and the use of secondary resources in powder metallurgy are promising directions of resource conservation [26–32].

In this paper, we present a new approach based on the carbonization of lignin in the presence of metallurgical dust to obtain magnetically sensitive carbon sorbents via an efficient solvent-free mechanochemical synthesis [9,34]. Our strategy is based on the use of dust as a filler, which plays the role of a graphitization catalyst and a porosity activator, and at the same time allows us to prepare magnetosensitive carbon sorbents. The advantage of such adsorbents is that in the contact purification of solutions, the use of magnetic sorbents greatly simplifies the separation of the sorbent by magnetic separation and the completeness of its processing [35,36]. The influence of the initial composition of lignin–magnetic dust blends on the textural, structural, thermal, and adsorption properties of final materials was evaluated. Adsorption studies regarding methylene blue on lignin–iron dust biochars were conducted. This work may expand ways to design and develop carbon sorbents and present a promising prospect for the application of carbon to wastewater decontamination.

## 2. Materials and Methods

### 2.1. Materials and Chemicals

The kraft lignin used in this study was from Indulin AT, MeadWestvaco Corp. (Charleston, SC, USA). The magnetic blast furnace dust was provided by the Blast furnace workshop of the Donetsk Metallurgical Plant Research. The hydrochloric acid (35–38%), sodium hydroxide, and sodium chloride were purchased from Chempur (Piekary Slaskie,

Poland). The methylene blue was bought from Merck (Darmstadt, Germany). All solutions were prepared using deionized water (0.05  $\mu\text{S}/\text{cm}$ , Polwater, Labpol, Cracow, Poland).

## 2.2. Materials Preparation

As in the previous paper [9], the materials were synthesized by mechanochemical activation and high-temperature pyrolysis. The first step of the procedure was a mechanochemical activation of kraft lignin and industrial waste magnetic iron dust blends that were loaded into a stainless-steel jar (250 mL) containing stainless steel balls with a 5 mm diameter for 2 h. The second stage was pyrolysis in a reactor at 800 °C and inert gas condition with a flow rate of 100 mL/min. The heating rate was 10 °C/min, and the samples were preserved in the reactor at the established temperature for 1 h, and then they were cooled at room temperature [9].

The names of the samples and the initial ratios of the components are given in Table 1.

**Table 1.** The ratios of the initial components used to prepare biochars.

Samples	Kraft Lignin (g)	Components Ratios		
		Kraft Lignin (%)	Magnetic Iron Dust (g)	Magnetic Iron Dust (%)
STInd-1	12.5	71.0	5.0	29.0
STInd-2	12.5	76.0	4.0	24.0
STInd-3	12.5	81.0	3.0	19.0
STInd-4	12.5	91.0	1.3	9.0
Indulin/Carbon	12.5	100.0	0.0	0.0

## 2.3. Methods

### 2.3.1. Low-Temperature Nitrogen Adsorption-Desorption

To determine the textural characteristics, the nitrogen adsorption–desorption isotherms at 77 K were recorded using a Micromeritics ASAP 2405N adsorption analyzer (Micrometric, Nocross, GA, USA). The specific surface area,  $S_{\text{BET}}$ , was calculated according to the standard BET method [37]. The total pore volume,  $V_p$ , was evaluated based on the nitrogen adsorption at  $p/p_0 = 0.98–0.99$  (where  $p$  and  $p_0$  denote the equilibrium and saturation pressure of nitrogen at 77 K, respectively). Nitrogen desorption data were used to compute pore size distributions (PSD, differential  $f_V(R) \sim dV_p/dR$  and  $f_S(R) \sim dS/dR$ ), using a model with slit-shaped pores [38]. Differential PSD concerning pore volume,  $f_V(R) \sim dV_p/dR$  and  $\int f_V(R)dR \sim V_p$ , were recalculated to incremental PSD (IPSD),  $\sum \Phi_{v,i}(R) = V_p$ . The  $f_V(R)$  and  $f_S(R)$  functions were also used to calculate the contributions of micropores ( $V_{\text{micro}}$  and  $S_{\text{micro}}$  at radius  $R \leq 1$  nm) and mesopores ( $V_{\text{meso}}$  and  $S_{\text{meso}}$  at  $1 \text{ nm} < R < 25$  nm).

### 2.3.2. Potentiometric Titration

Potentiometric titration was performed using a system composed of a 765 Dosimat Metrohm autoburet (Herisau, Switzerland), a PHM240 Radiometer pH-meter (Copenhagen, Denmark), an Ecoline RE207 thermostat (Lauda, Germany) to maintain the 25 °C temperature, a degassing system (an inert gas atmosphere), and a 50 mL quartz container. Thirty mL of 0.1 mol/L electrolyte (sodium chloride), 0.3 mL of 0.2 mol/L hydrochloric acid, and 0.1 g of solid sample (biochar) were added to the quartz vessel to conduct the experiment. After achieving a constant temperature and pH value, the 0.1 mol/L sodium hydroxide was gradually titrated. Analogous titration was performed without the addition of the solid. Based on the collected data, the surface charge and the point of zero charge ( $\text{pH}_{\text{PZC}}$ ) were established for all carbonized samples [9].

### 2.3.3. X-ray Diffraction (XRD)

The XRD patterns were recorded using a DRON UM1 diffractometer (Burevestnik, Saint Petersburg, Russia) at  $2\theta$  from 10 to 90° with filtered Co  $K_\alpha$  radiation and Bragg–Brentano geometry.

### 2.3.4. X-ray Fluorescence (XRF)

The XRF was used for an elemental composition analysis of bulk samples using an Expert 3L XRF desktop high-precision express analyzer in helium atmosphere.

### 2.3.5. Raman Spectroscopy

The Raman spectra were recorded at 3200–150 cm<sup>−1</sup> using Via Reflex Microscope DMLM Leica Research Grade, Reflex (Renishaw, UK) with laser excitation at λ<sub>0</sub> = 785 nm.

### 2.3.6. Thermal Analysis (TA)

The thermogravimetric (TG) measurements with differential thermal analysis (DTA) of samples (with a mass of 100–150 mg) placed in a ceramic crucible were performed at a temperature range between 25 and 1000 °C in the air atmosphere using a Derivatograph Q 1500D (Paulik, Paulik & Erdely, MOM, Budapest, Hungary) with a heating rate of 10 °C/min.

### 2.3.7. Equilibrium Adsorption Studies

Adsorption equilibrium studies of methylene blue (MB) on indulin–magnetic dust adsorbents were carried out using a Carry 4000, Varian UV-Vis spectrophotometer (Melbourne, Australia). Adsorbent with a mass of 0.05 g was placed into a 100 mL conical flask. Then, 50 mL of methylene blue aqueous solutions (pH ~7) with initial concentrations from 0.005 to 0.1 mmol/L (1.6 to 32 mg/L) were shaken for 2 days at 25 °C with 110 rpm in a New Brunswick Scientific Shaker (Edison, NJ, USA). When equilibrium was established, the absorbance was measured at 450–200 nm, and the methylene blue concentration was evaluated based on the maximum of the absorbance peak. The adsorbed amount (*a*) was determined using the Mass Balance Equation (1), and the percentages of removal of methylene blue from solutions were determined applying Equation (2). The adsorption data were analyzed based on modified Langmuir (3) and Freundlich (4) isotherms.

$$a = \frac{(c_0 - c_{eq}) \cdot V}{m} \quad (1)$$

$$\% \text{ removal}_{MB} = \frac{(c_0 - c_{eq})}{C_0} \cdot 100 \quad (2)$$

$$a = a_m \frac{K_{ML} \cdot C_{eq}}{(C_S - C_{eq}) + (K_{ML} \cdot C_{eq})} \quad (3)$$

$$a = K_F \cdot C_{eq}^{\frac{1}{n}} \quad (4)$$

where *a* is the adsorption amount at equilibrium (mg/g); *C*<sub>0</sub> is the initial concentration of dye (mg/L); *C*<sub>eq</sub> is the equilibrium concentration of dye (mg/L); *V* is the volume of solution; *m* is the mass of adsorbent; % *removal*<sub>MB</sub> is the percentage of methylene blue removal; *a*<sub>*m*</sub> is the maximum adsorption amount; *K*<sub>*ML*</sub> is the modified Langmuir equilibrium constant; *C*<sub>*S*</sub> is the value of saturated concentration of solute [mg/L], (dimensionless quantity); *K*<sub>*F*</sub> is the Freundlich constant (mg/g); and *n* is the heterogeneity factor.

The influence of pH and contact time were checked before the adsorption studies of methylene blue. The effect of pH on the percent of methylene blue removal was taken into account. Biochars with a mass of 0.05 g were placed in 100 mL plastic containers and contacted with 50 mL of 12.8 mg/L methylene blue solution at pH 2, 4, 7, and 10. The pH value was preserved by adding 0.1 mol/L hydrochloric acid or 0.1 mol/L sodium hydroxide solutions and shaken for 2 days at 25 °C with 110 rpm in a New Brunswick Scientific Shaker to achieve equilibrium. Additionally, the effect of time was examined on two selected materials, including STInd-1 and STInd-4. The samples of mass of 0.05 g were situated in 100 mL Erlenmeyer flasks and contacted with 50 mL of 12.8 mg/L at pH ~7, and the solution was measured at appropriate time intervals. In all cases, the adsorbent was



centrifuged for 10 min with 10,000 rpm at 25 °C using an MPW-352R centrifuge (Warsaw, Poland), and the supernatant was analyzed [9].

### 3. Results and Discussion

#### 3.1. Low-Temperature Nitrogen Adsorption-Desorption

Nitrogen adsorption–desorption isotherms were collected to verify the textural properties of biochars (Figure 1a). The specific surface area ( $S_{BET}$ ) of carbonized indulin–iron dust materials is in the range between 290 and 330 m<sup>2</sup>/g, while pyrolyzed indulin is characterized by a specific surface area of only 7 m<sup>2</sup>/g. The adsorption–desorption data are summarized in Table 2.

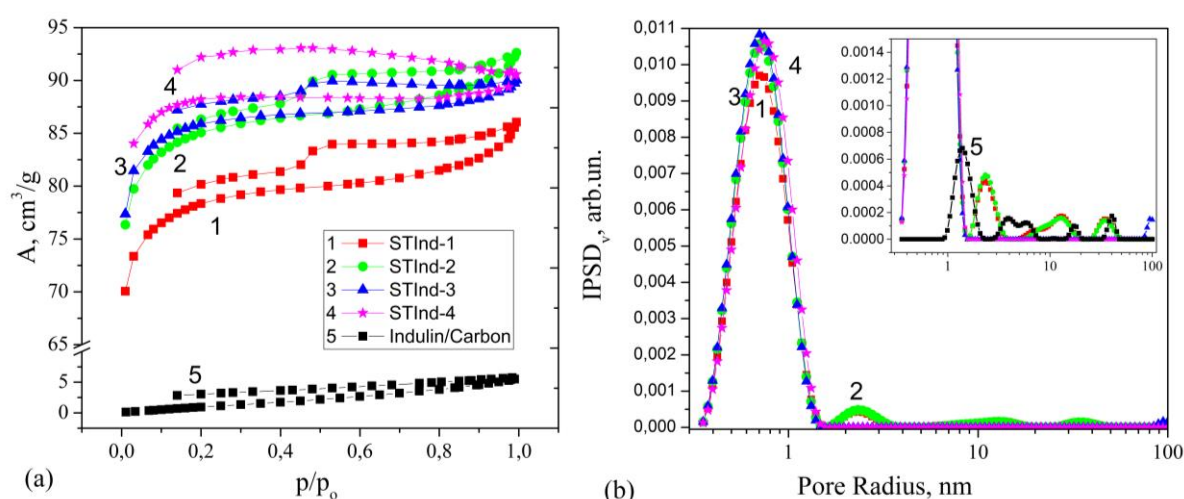


**Figure 1.** (a) Nitrogen adsorption–desorption isotherms and (b) pore size distributions of 1: STInd–1; 2: STInd–2; 3: STInd–3; 4: STInd–4; and 5: indulin/carbon.

**Table 2.** Textural characteristics of biochars.

Sample	$S_{BET}$ (m <sup>2</sup> /g)	$V_{micro}$ (cm <sup>3</sup> /g)	$V_{meso}$ (cm <sup>3</sup> /g)	$V_p$ (cm <sup>3</sup> /g)	$V_{micro}/V_p$	$V_{meso}/V_p$
STInd–1	290	0.118	0.014	0.132	0.894	0.106
STInd–2	315	0.128	0.014	0.142	0.901	0.099
STInd–3	313	0.129	0.011	0.140	0.921	0.079
STInd–4	330	0.131	0.008	0.139	0.942	0.058
Indulin/Carbon	7	–	0.007	0.007	–	–

The nitrogen adsorption–desorption isotherms of the indulin-based samples can be ascribed as a mixture of I and IV types with a combination of the hysteresis loops of H1 and H4 according to IUPAC classification, which is associated with the occurrence of microporous and mesoporous structures of biochar surfaces. The desorption curves of the STInd–1, STInd–2, and STInd–3 samples show an inflection point in the relative pressure range between 0.4 and 0.6, which indicates that a high amount of adsorbed gas is instantly desorbed due to the presence of special ink bottle-like pore structures or the deformation of the coal body by filler [39,40].

The adsorption and desorption curves of the STInd–4 sample do not come together at a relatively low pressure in the isotherm. This may be caused by the irreversible uptake of nitrogen molecules in pores through very narrow pore entrances and some swelling of the adsorbents. The micropores are extremely developed in this sample, and their pore area gives a majority share to the total pore area. The STInd–4 sample shows a higher surface area than STInd–1 which is most likely due to the partial pore blocking by the filler. Generally, a small decrease in  $S_{BET}$ ,  $V_{mic}$  values is observed with an increase in the filler

content, and the mesopore volume increases at the same time. The pore size distribution curves (Figure 1b with insert Table 2) show that the pore size distributions are mostly in the microporous range, which indicates that the resulting carbons have a microporous structure; however, the mesopores of different sizes also contribute to the total porosity.

### 3.2. X-ray Investigations

The main chemical composition of the blast furnace dust probe was analyzed using X-ray fluorescence, and the data are presented in Table 3.

**Table 3.** The chemical composition of the blast furnace dust.

Component	Fe	Ca	Si	Cl	S	Mg	Mn	Pb	Zn	Al
Content (wt%)	79.763 ( $\pm 0.100$ )	9.965 ( $\pm 0.031$ )	3.951 ( $\pm 0.080$ )	3.843 ( $\pm 0.050$ )	2.166 ( $\pm 0.058$ )	0.134 ( $\pm 0.010$ )	0.089 ( $\pm 0.017$ )	0.045 ( $\pm 0.006$ )	0.027 ( $\pm 0.004$ )	0.015 ( $\pm 0.003$ )

According to the XRF and XRD data (Tables 3 and 4 and Figure 2), it can be concluded that the main components of the blast furnace dust include the  $\text{Fe}_3\text{O}_4$ ,  $\alpha\text{-Fe}_2\text{O}_3$ ,  $\text{SiO}_2$ , and  $\text{CaCO}_3$  phases. The sample does not contain appreciable amounts of Pb and Zn as was reported by Das B. et al. [31] for samples from other parts of the world. The carbonization of indulin–iron dust blends at 800 °C; therefore, iron oxides are partly reduced to  $\alpha\text{-Fe}$ . Furthermore, FeO and  $\text{Fe}_3\text{O}_4$  phases are also present in small amounts. In addition to amorphous carbon, graphite is observed in carbonized samples as evidenced by the presence of the (002) peak at  $2\theta = 31^\circ$ . Data regarding the phase composition are given in Table 4. The highest content of amorphous carbon is in the STInd–4 sample.

**Table 4.** Structural characteristics of biochars.

Sample	Phase Composition	Center ( $\text{cm}^{-1}$ )		FWHM ( $\text{cm}^{-1}$ )		$I_D/I_G$	Carbon Content (%)
		D	G	D	G		
DustST	$\text{Fe}_3\text{O}_4$ , $\alpha\text{-Fe}_2\text{O}_3$ , $\text{SiO}_2$ , $\text{CaCO}_3$	-	-	-	-	-	-
STInd–1	Fe, FeO, $\text{Fe}_3\text{O}_4$ , $\text{SiO}_2$ , $\text{C}_{\text{amorph}}$	1310	1600	84.8	57.2	0.9	46.0
STInd–2	Fe, FeO, $\text{Fe}_3\text{O}_4$ , C $\text{SiO}_2$ , $\text{C}_{\text{amorph}}$	1312	1598	120.3	64.6	1.0	51.0
STInd–3	Fe, FeO, $\text{Fe}_3\text{O}_4$ , C $\text{SiO}_2$ , $\text{C}_{\text{amorph}}$	1314	1598	120.8	64.7	1.2	56.0
STInd–4	Fe, $\text{Fe}_3\text{O}_4$ , FeO, $\text{SiO}_2$ , $\text{C}_{\text{amorph}}$	1316	1598	121.5	63.2	1.3	66.0
Indulin/Carbon	$\text{C}_{\text{amorph}}$	1319	1586	90.5	58.1	1.2	100.0

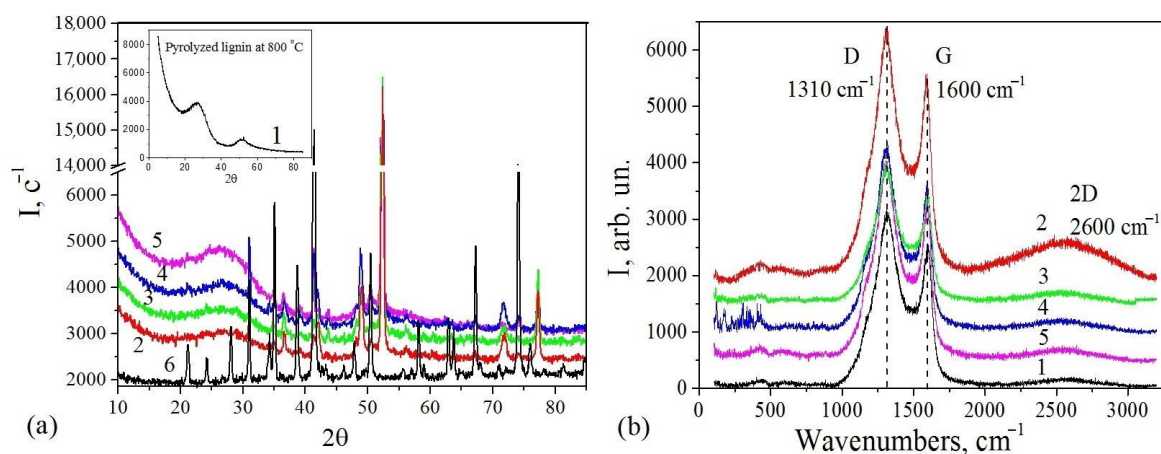


**Figure 2.** (a) XRD patterns and (b) Raman spectra of carbonized materials and furnace dust. 1: indulin/carbon; 2: STInd–1; 3: STInd–2; 4: STInd–3; 5: STInd–4; and 6: DustST.

The formation of Zn and Mn ferrite phases as well as  $\text{Al}_2\text{O}_3$ ,  $\text{MgO}$ , and  $\text{Ca}_2\text{SiO}_4$  (as was reported by Li et al. [41]) cannot be precisely established to see the crystalline compounds due to the sensitivity of this method and their very low content. As shown in Figure 2a (insertion), the pyrolyzed lignin is amorphous due to the presence of two broad and non-intense maxima of the halo at around  $2\theta = 26^\circ$  and  $50^\circ$  in the pattern that is characteristic of amorphous carbon.

Additional information about the carbon phase in biochar is provided by the Raman spectroscopy. As can be seen in Figure 2b, the Raman spectra show characteristic D and G peaks with the maxima at wavenumbers of  $\sim 1310$  and  $\sim 1600\text{ cm}^{-1}$ , respectively. The G band is due to bond stretching of all pairs of  $\text{sp}^2$  atoms in both rings and chains and is associated with the vibration of the ideal graphite lattice ( $\text{E}_{2g}$  symmetry, C-C in-plane stretching mode), while the D band is due to the breathing modes of  $\text{sp}^2$  atoms in rings ( $\text{A}_{1g}$  symmetry) [42]. The wide intensive G band in the samples indicates the increasing degree of carbon disordering.

The intensity ratio of the D and G peaks ( $I_D/I_G$ ) is commonly used to measure the degree of graphitization of carbon structures. Only STInd-1 and STInd-2 samples have an  $I_D/I_G$  ratio  $\leq 1$  (Table 4), whereas other STInd samples have values above 1, which indicates the presence of amorphous phases. This value is higher than or comparable to previously reported data [43]. Apart from the D and G peaks, a 2D peak appears at regions  $2200\text{--}2800\text{ cm}^{-1}$  as the overtones of fundamental modes, which was assigned by Y. Wang et al. as a highly ordered pyrolytic graphite [44]. Moreover, the D band maximum moves toward the higher wavenumber, and the broadening of FWHM of all peaks takes place due to increasing disordering via changes in the crystallite structure (i.e., the arrangement or reconstruction of a boundary carbon atom) (Figure 2b). Thus, an increase in the filler content leads to an intensifying of the crystallinity of the graphite-like fraction.

### 3.3. Thermal Analysis

Weight losses in the temperature range of  $25\text{--}1000^\circ\text{C}$  is observed on the TG curves during the thermo-oxidative destruction of the samples. The first mass loss, which is visible on the TG curves for all samples (Figure 3) at a temperature of  $\sim 100^\circ\text{C}$ , corresponds to the desorption of physisorbed water. This low temperature weight loss is not accompanied by DTA effects, but it is clearly visible on the DTG curves. Moreover, it can be seen that TG and DTA shift toward higher temperatures with an increase in the content of magnetic fillers in the samples.

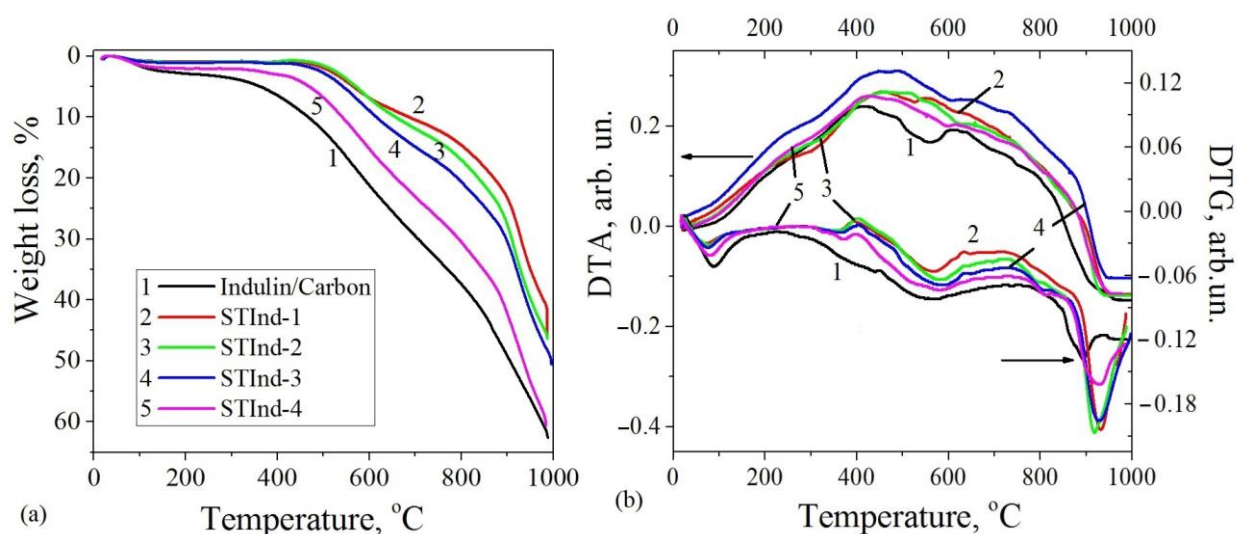


Figure 3. TG (a) and DTG and DTA (b) curves of biochars.



The DTA curves of modified samples have a broad peak in the temperature range of 200–950 °C and consist of several overlapping peaks that result from a series of processes, including the adsorption of oxygen on carbon and metals (at  $T > 200$  °C) and carbon combustion with CO<sub>2</sub> removal (DTA<sub>max</sub> at 400–800 °C). The DTG curves demonstrate that three mass loss steps occurred during the thermal degradation of the modified samples in this region. The weight decrease phenomenon that is visible in this range on the TG curves is due to the decomposition of functional groups of biochars [45,46], the oxidation of metal nano-particles in the air with the formation of oxides forms above 700 °C, and the thermo-oxidations of graphene structures on the surface of biochar. When comparing the TG and DTA curves of indulin/carbon to the modified samples, the magnetic dust filler gives the carbons a higher thermal resistance. The wide temperature range of the oxidation of modified samples can be explained by the presence of carbon nanoparticle aggregates of higher densities. According to the literature [8,47], the presence of two exothermic peaks on the DTA curves (during analysis in a static atmosphere in air) is related to the oxidation of carbon atoms on the surface and oxygen diffusion and reaction in the pores. The distinctive T<sub>max</sub> at temperatures above 800 °C can be attributed to the high external thermal energy that must be applied to the system to overcome strong bonding in the carbon lattice structures. The low T<sub>max</sub> in the indulin/carbon indicates that less heat energy is necessary to destroy the weak non-graphitic sp<sup>3</sup> hybridized carbon atoms with a high density of defects during thermooxidative reactions compared with STInd-1 and STInd-2 samples; in these samples, sp<sup>2</sup> hybridized carbon atoms are ordered by covalent bonds in a hexagonal carbon framework. These results correspond precisely with the Raman spectroscopy data. Moreover, weight loss at temperatures above 800 °C can be associated with the decomposition of residual ash, the volatilization of heavy metals, and further oxidation of metals.

The carbon retention of lignin is 65 wt.%, which indicates a high yield of carbon and the prospect of its use for obtaining carbon biochars by pyrolysis. The carbon content in the carbonized samples was calculated [48] according to the TG data and took into account the fact that DustST contains ~20% impurities (Table 4).

### 3.4. Potentiometric Titration

Potentiometric titration was used to determine the acid base properties of indulin–iron dust biochars. The surface charge dependences as a function of pH are presented in Figure 4. The values of the pH<sub>PZC</sub> (point of zero charge) of the STInd-1, STInd-2, STInd-3, STInd-4, and indulin/carbon samples are 7.38, 7.81, 8.32, 8.58, and 9.41, respectively. All examined carbonized materials are positively and negatively charged and can interact with both cations and anions, depending on the pH region. Overall, the pH<sub>PZC</sub> values reveal the alkaline nature of the carbonized materials; moreover, the alkaline properties decrease with iron magnetic dust filler content. This result may be related to a lower degree of carbonization with an increasing filler amount. Generally, the potentiometric titration results are in good agreement with data obtained by Raman spectroscopy, X-ray diffraction, and thermal analysis. Besides, a good correlation between the percentage of carbon and pH<sub>PZC</sub> were found since the pH<sub>PZC</sub> is higher when the carbon content in the pyrolyzed material is higher [9].

### 3.5. Adsorption Studies

The adsorption properties of carbonized indulin–iron dust materials were tested using a cationic thiazine dye known as methylene blue. The measurements of adsorption isotherms were conducted using a wide pH range.

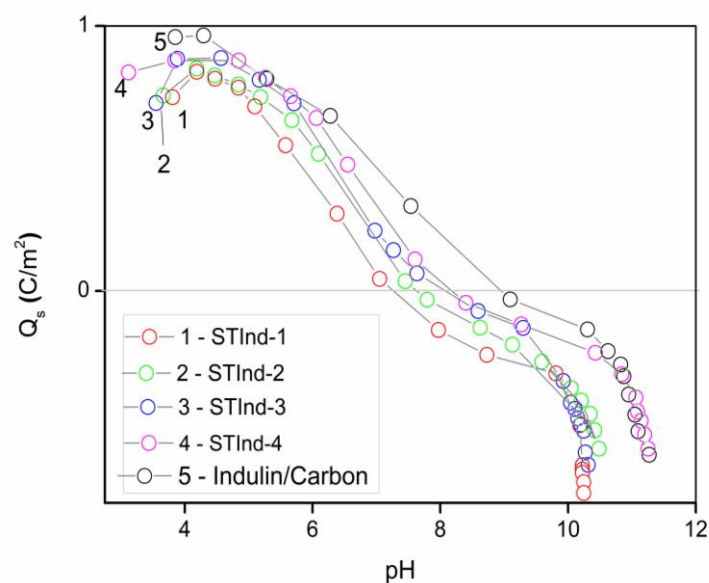


**Figure 4.** Surface charge density as a function of pH ( $Q_s$  vs. pH) of carbonized indulin-based biochars.

The effect of pH on the removal of methylene blue from solutions with an initial concentration of 12.8 mg/L is presented in Figure 5a. It can be seen that pH only slightly affects adsorption efficiency. The effect of contact time on the adsorption of methylene blue from solutions at pH ~7 on the selected carbonized materials is visible in Figure 5b. It can be concluded that the adsorption equilibrium is achieved in 1 day. The percentage of methylene blue removal by indulin-based adsorbents from solutions at pH ~7 is shown in Figure 5c. It is visible that the change in the value of the removed substance is related to the adsorbent structural and surface properties. Generally, the adsorption data reveal a meaningful increase in the adsorption uptake for materials with iron dust filler (STInd-1, STInd-2, STInd-3, and STInd-4) compared with the sample with pyrolyzed indulin (indulin/carbon) which shows a very weakly developed pore structure. The carbonized indulin samples with the addition of the magnetic filler are characterized by high values of specific surface area ( $S_{BET}$ ) of ~300 m<sup>2</sup>/g, while indulin is only 7 m<sup>2</sup>/g. Taking into account the filler influence, the effectiveness of the adsorption process may be ordered as follows: STInd-1 > STInd-2 > STInd-3 > STInd-4. The differences in adsorption capacity can be related, firstly, to the structure characteristics (e.g., the specific surface area, microporosity, and mesoporosity contribution) and, secondly, to the surface properties (i.e., the acid base properties). The share of mesopores in the STInd-1 sample is the highest (0.106), and the micropores share is the lowest (0.894). On the contrary, for STInd-4, the contribution of mesopores is the lowest (0.058), and micropores share is the highest (0.942). The mesoporosity gradually diminishes as the filler content of the initial mixture of blends decreases. It may be that the presence of mesopores facilitates the penetration of the internal adsorbent space by a large molecule of dye.

The parameters calculated based on modified Langmuir [49] and Freundlich isotherms are summarized in Table 5. Both equations show correlation coefficients above 0.9, which allows them to be used to characterize the adsorption process. The tests show that the maximum adsorption of methylene blue for the indulin–lignin dust biochars is 10 to 20 times higher than that of the reference sample (indulin/carbon) (Figure 5d).

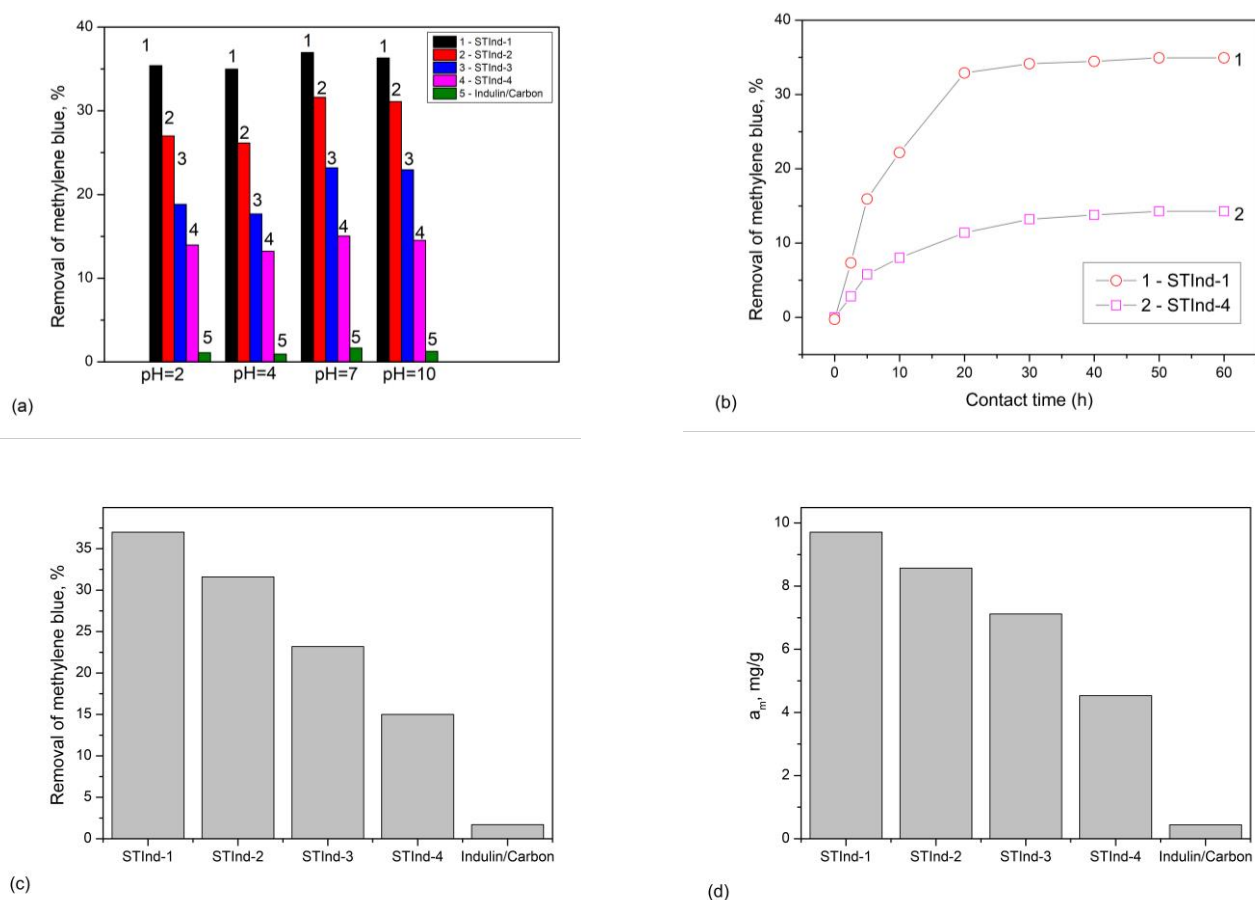


**Figure 5.** The effect of (a) pH ( $C_0 = 12.8$  mg/L, pH = 2, 4, 7), (b) contact time ( $C_0 = 12.8$  mg/L, pH = 7), (c) the percent of methylene blue removal ( $C_0 = 12.8$  mg/L, pH ~7) and (d) maximum adsorption ( $a_m$ ) (mg/g) for the investigated adsorbents.

**Table 5.** Parameters of modified Langmuir and Freundlich isotherms for methylene blue adsorption on biochars.

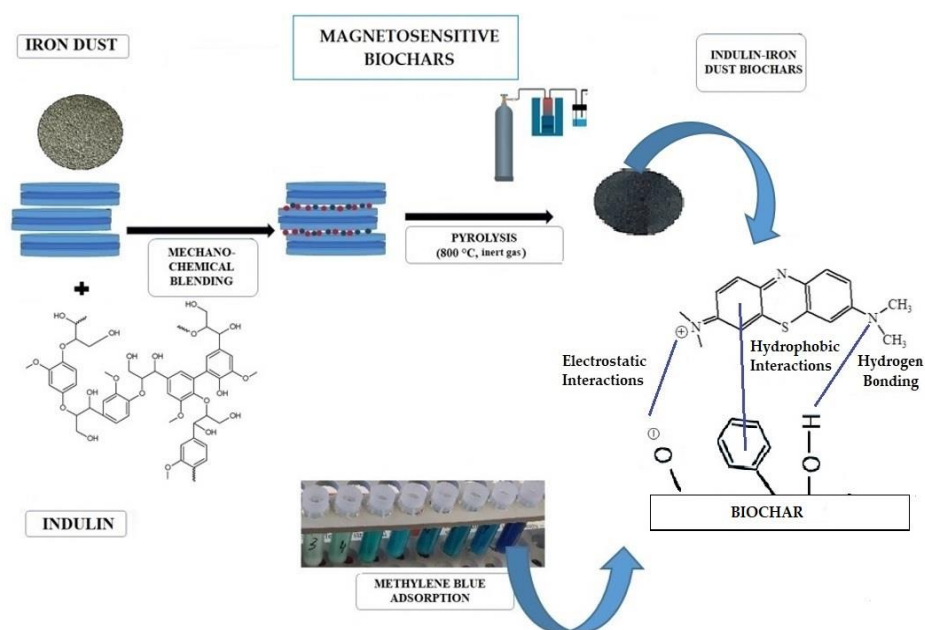
Sample	Modified Langmuir Isotherm			Freundlich Isotherm		
	$R^2$	$K_{ML}$ (Dimensionless)	$a_m$ (mg/g)	$R^2$	$K_F$ (mg/g)	$N$
STInd-1	0.911	4336	9.71	0.933	0.949	1.49
STInd-2	0.980	5139	8.57	0.953	1.045	1.66
STInd-3	0.905	4285	7.12	0.951	0.838	1.72
STInd-4	0.979	5960	4.53	0.972	0.669	1.89
Indulin/Carbon	0.988	5,889,834	0.44	0.184	0.361	12.71

The results of the literature overview regarding the adsorption of methylene blue on biochars and commercially available activated carbons are shown in Table 6. One can state that the indulin–iron dust materials show comparable or, in some cases, even higher adsorption effectiveness toward methylene blue solutions compared with other biochars. Besides, it has been reported that lignin-based biochars with the addition of magnetic filler show a higher adsorption efficiency than carbonized lignin [3,9,50–57].

**Table 6.** Comparison of literature data regarding methylene blue adsorption on biochars and commercial activated carbons.

Lp.	Sample	$a_m$ (mg/g)	Literature
1	Zeolite-Waste Materials	10	[3]
2	Tannin/Bentonite-Derived Biochar (TBC-3)	5	[9]
3	Compost Biochar	13	[50]
4	Biomass Biochar	12	[50]
5	Optimal Biochar from Argan Shells Powder	31	[51]
6	Biochar from Pongamia Glabra Seed Cover	2	[52]
7	Ouricuri Endocarp Biochar	2	[53]
8	Biochar from Anaerobic Digestion Residue (BC-R)	10	[54]
9	Biochar from Palm Bark (BC-PB)	3	[54]
10	Biochar from Eucalyptus (BC-E)	2	[54]
11	Composite Based on Ca/Al Layered Double Hydroxide-biochar	19	[55]
12	GAC	131	[56]
13	CAC	980	[57]

Regarding the adsorption mechanisms of the studied systems (i.e., biochar and methylene blue), one can take into account mainly hydrophobic and electrostatic interactions, but also hydrogen bonding. The scheme of biochars synthesis with the possible mechanisms of methylene blue adsorption is presented in Figure 6. Methylene blue is a positively charged molecule which may interact electrostatically with negatively charged or electron-rich moieties. The formation of hydrogen bonding between hydrogen containing groups (Si-O-H, Me-O-H, C-O-H) and nitrogen atoms of methylene blue can also occur. One can expect that the  $\pi$ - $\pi$  interactions between the aromatic rings of dye molecules and graphene structures of biochars prevail [9].

**Figure 6.** The scheme of biochars synthesis with the possible mechanism of methylene blue adsorption.

#### 4. Conclusions

The present work successfully explored the potential utilization of abundant lignin and industrial magnetic dust as precursors to magneto-sensitive carbon systems. Lignin and industrial magnetic dust blends were successfully converted into magnetic carbon sorbents via catalytic carbonization. The synthesized indulin–iron dust biochars exhibited surface areas of  $\sim 300 \text{ m}^2/\text{g}$  and a high degree of microporosity with a certain mesoporosity

contribution and high thermal stability. Compared with the indulin–iron dust biochars, the carbonized inulin was characterized by a surface area of only 7 m<sup>2</sup>/g.

The obtained materials showed a maximum adsorption in a range between 4.53 and 9.71 mg/g toward methylene blue, while it was only 0.44 mg/g for pyrolyzed indulin. A strong increase in adsorption uptake was observed for materials that contained iron dust filler. The differentiation of adsorption effectiveness was related to structure and surface characteristics. The best adsorption properties were found for the STInd-1 material with 29% iron filler content and the highest share of mesopores in the pore structure. However, other materials with a lower filler content (9–24%) and a lower contribution of micropores also showed quite good adsorption efficiency.

The utility of magnetosensitive sorbents may be very promising regarding the purification of waters; therefore, reducing the cost of magnetite for its synthesis is an urgent task. Thus, production that uses iron-containing wastes seems to be a very effective method. Overall, this study expands the understanding of the development of lignin-derived magnetosensitive biochar as a renewable substitute for commercial carbons in various industries.

**Author Contributions:** Conceptualization, M.G. and M.B.; material synthesis, M.G. and M.B.; investigation, M.G., A.B., D.S., M.B. and O.O.; methodology, M.G., A.B., D.S., O.O., M.B., V.G. and A.D.-M.; writing—original draft, M.G., A.B., D.S., O.O. and M.B.; writing—review and editing, A.D.-M. and V.G. All authors have read and agreed to the published version of the manuscript.

**Funding:** This research received no external funding.

**Institutional Review Board Statement:** Not applicable.

**Informed Consent Statement:** Informed consent was obtained from all subjects involved in the study.

**Data Availability Statement:** The data and samples are available from the authors.

**Acknowledgments:** This work was implemented within the Scholarship of the International Visegrad Fund (contract number 52211439).

**Conflicts of Interest:** The authors declare no conflict of interest.

## References

1. Budarin, H.L.V.; Clark, J.H. Rapid and Efficient Adsorption of Methylene Blue Dye From Aqueous Solution by Hierarchically Porous, Activated Starbons®: Mechanism and Porosity Dependence. *J. Hazard. Mater.* **2022**, *436*, 129174. [\[CrossRef\]](#)
2. Chen, J.; Tang, C.; Li, X.; Sun, J.; Liu, Y.; Huang, W.; Wang, A.; Lu, Y. Preparation and Modification of Rape Straw Biochar and Its Adsorption Characteristics for Methylene Blue in Water. *Water* **2022**, *14*, 3761. [\[CrossRef\]](#)
3. Imessaoudene, A.; Cheikh, S.; Bollinger, J.C.; Belkhir, L.; Tiri, A.; Bouzaza, A.; El Jery, A.; Assadi, A.; Amrane, A.; Mouni, L. Zeolite Waste Characterization and Use as Low-Cost, Ecofriendly, and Sustainable Material for Malachite Green and Methylene Blue Dyes Removal: Box–Behnken Design, Kinetics, and Thermodynamics. *Appl. Sci.* **2022**, *12*, 7587. [\[CrossRef\]](#)
4. Zamouchea, M.; Mouni, L.; Ayachia, A.; Merniza, I. Use of commercial activated carbon for the purification of synthetic water polluted by a pharmaceutical product. *Desalination Water Treat.* **2019**, *172*, 86–95. [\[CrossRef\]](#)
5. Zhu, S.; Khan, M.A.; Kameda, T.; Xu, H.; Wang, F.; Xia, M.; Yoshioka, T. New insights into the capture performance and mechanism of hazardous metals Cr<sup>3+</sup> and Cd<sup>2+</sup> onto an effective layered double hydroxide based material. *J. Hazard. Mater.* **2022**, *426*, 128062. [\[CrossRef\]](#)
6. Bosacka, A.; Zienkiewicz-Strzalka, M.; Wasilewska, M.; Derylo-Marczewska, A.; Podkoscielna, B. Physicochemical and Adsorption Characteristics of Divinylbenzene-co-Triethoxyvinylsilane Microspheres as Materials for the Removal of Organic Compounds. *Molecules* **2021**, *26*, 2396. [\[CrossRef\]](#)
7. Bosacka, A.; Zienkiewicz-Strzalka, M.; Derylo-Marczewska, A.; Chrzanowska, A.; Wasilewska, M.; Sternik, D. Physicochemical, structural, and adsorption properties of chemically and thermally modified activated carbons. *Colloids Surf. A Physicochem. Eng. Asp.* **2022**, *647*, 129130. [\[CrossRef\]](#)
8. Derylo-Marczewska, A.; Sternik, D.; Swiatkowski, A.; Kusmier, K.; Gac, W.; Buczek, B. Adsorption of phenol from aqueous and cyclohexane solutions on activated carbons with differentiated surface chemistry. *Thermochim. Acta* **2022**, *715*, 179299. [\[CrossRef\]](#)
9. Galaburda, M.; Bosacka, A.; Sternik, D.; Bogatyrov, V.; Oranska, O.; Gun'ko, V.M.; Derylo-Marczewska, A. Development, Synthesis and Characterization of Tannin/Bentonite-Derived Biochar for Water and Wastewater Treatment from Methylene Blue. *Water* **2022**, *14*, 2407. [\[CrossRef\]](#)
10. Norgren, M.; Edlund, H. Lignin: Recent advances and emerging applications. *Curr. Opin. Colloid Interface Sci.* **2014**, *19*, 409–416. [\[CrossRef\]](#)



11. Kakroodi, A.R.; Sain, M. Lignin-Reinforced Rubber Composites. In *Lignin in Polymer Composites*, 1st ed.; Faruk, O., Sain, M., Eds.; William Andrew Elsevier: Amsterdam, The Netherlands, 2016; pp. 195–206. [CrossRef]
12. Mammari, A.C.; Mouni, L.; Bollinger, J.C.; Belkhiri, L.; Bouzaza, A.; Assadi, A.A.; Belkacemi, H. Modeling and optimization of process parameters in elucidating the adsorption mechanism of Gallic acid on activated carbon prepared from date stones. *Sep. Sci. Technol.* **2020**, *55*, 3113–3125. [CrossRef]
13. Bouchelkia, N.; Mouni, L.; Belkhiri, L.; Bouzaza, A.; Bollinger, J.C.; Madani, K.; Dahmoune, F. Removal of lead(II) from water using activated carbon developed from jujube stones, a low-cost sorbent. *Sep. Sci. Technol.* **2016**, *51*, 1645–1653. [CrossRef]
14. Chatterjee, S.; Saito, T. Lignin-Derived Advanced Carbon Materials. *ChemSusChem* **2015**, *8*, 3941–3958. [CrossRef] [PubMed]
15. Kane, S.; Ulrich, R.; Harrington, A.; Stadie, N.P.; Ryan, C. Physical and chemical mechanisms that influence the electrical conductivity of lignin-derived biochar. *Carbon Trends* **2021**, *5*, 100088. [CrossRef]
16. Zhu, L.; Liu, X.; Wu, Y.; Wang, Q.; Wang, H.; Li, D. Fast-pyrolysis lignin-biochar as an excellent precursor for high-performance capacitors. *Renew. Energy* **2022**, *198*, 1318–1327. [CrossRef]
17. Demir, M.; Tessema, T.; Farghaly, A.A.; Nyankson, E.; Saraswat, S.K.; Aksoy, B.; Islamoglu, T.; Collinson, M.M.; El-Kaderi, H.M.; Gupta, R. Lignin-derived heteroatom-doped porous carbons for supercapacitor and CO<sub>2</sub> capture applications. *Int. J. Energy Res.* **2018**, *42*, 2686–2700. [CrossRef]
18. Demir, M.; Kahveci, Z.; Aksoy, B.; Palapati, N.K.R.; Subramanian, A.; Cullinan, H.T.; El-Kaderi, H.M.; Harris, C.T.; Gupta, R.B. Graphitic Biocarbon from Metal-Catalyzed Hydrothermal Carbonization of Lignin. *Ind. Eng. Chem. Res.* **2015**, *54*, 10731–10739. [CrossRef]
19. Yi, Z.; Li, C.; Zhang, L.; Zhang, S.; Gao, W.; Wang, S.; Li, B.; Hu, X. Impacts of CO<sub>2</sub> atmosphere on property of the biochar from pyrolysis of lignin. *J. Anal. Appl. Pyrolysis* **2022**, *167*, 105689. [CrossRef]
20. Dai, Q.; Liu, Q.; Zhang, X.; Cao, L.; Hu, B.; Shao, J.; Ding, F.; Guo, X.; Gao, B. Synergetic effect of co-pyrolysis of sewage sludge and lignin on biochar production and adsorption of methylene blue. *Fuel* **2022**, *324*, 124587. [CrossRef]
21. Wu, F.; Chen, L.; Hu, P.; Zhou, X.; Zhou, H.; Wang, D.; Lu, X.; Mi, B. Comparison of properties, adsorption performance and mechanisms to Cd(II) on lignin-derived biochars under different pyrolysis temperatures by microwave heating. *Environ. Technol. Innov.* **2022**, *25*, 102196. [CrossRef]
22. Liu, D.; Gu, W.; Zhou, L.; Lei, J.; Wang, L.; Zhang, J.; Liu, Y. From biochar to functions: Lignin induced formation of Fe<sub>3</sub>C in carbon/Fe composites for efficient adsorption of tetracycline from wastewater. *Sep. Purif. Technol.* **2023**, *304*, 122217. [CrossRef]
23. Liu, X.J.; Li, M.F.; Singh, S.K. Manganese-modified lignin biochar as adsorbent for removal of methylene blue. *J. Mater. Res. Technol.* **2021**, *12*, 1434–1445. [CrossRef]
24. Li, Y.; Wang, F.; Miao, Y.; Mai, Y.; Li, H.; Chen, X.; Chen, J. A lignin-biochar with high oxygen-containing groups for adsorbing lead ion prepared by simultaneous oxidization and carbonization. *Bioresour. Technol.* **2020**, *307*, 123165. [CrossRef]
25. Sun, Y.; Wang, T.; Sun, X.; Bai, L.; Han, C.; Zhang, P. The potential of biochar and lignin-based adsorbents for wastewater treatment: Comparison, mechanism, and application—A review. *Ind. Crops Prod.* **2021**, *166*, 113473. [CrossRef]
26. World Steel Association AISBL. Available online: <https://worldsteel.org/steel-topics/statistics/world-steel-in-figures-2022> (accessed on 10 November 2022).
27. World Steel Association AISBL. Available online: <https://worldsteel.org/publications/policy-papers/co-product-position-paper/2022> (accessed on 10 November 2022).
28. Nayak, N.P. Characterization of blast furnace flue dust- an assessment for its utilization. *Mater. Today. Proc.* **2022**, *50*, 2078–2083. [CrossRef]
29. Lepa, V.V.; Prognimak, O.D. Blast Furnace Slag Disposal Problems in the Context of the Transition to a Circular Economy. *Econ. Her. Donbass* **2021**, *1*, 129–145. [CrossRef]
30. Özbay, E.; Erdemir, M.; Durmu, H. Utilization and efficiency of ground granulated blast furnace slag on concrete properties—A review. *Constr. Build. Mater.* **2016**, *105*, 423–434. [CrossRef]
31. Das, B.; Prakash, S.; Reddy, P.S.R.; Biswal, S.K.; Mohapatra, B.K.; Misra, V.N. Effective utilization of blast furnace flue dust of integrated steel plants. *Eur. J. Miner. Process. Environ. Prot.* **2002**, *2*, 61–68.
32. Li, Y.; Liu, Y.; Gong, X.; Nie, Z.; Cui, S.; Wang, Z.; Chen, W. Environmental impact analysis of blast furnace slag applied to ordinary Portland cement production. *J. Clean. Prod.* **2016**, *120*, 221–230. [CrossRef]
33. Drachuk, Y.; Stalinskaya, E.; Snitko, E.; Zavgorodnyaya, E.; Jaworska, M.; Savyuk, L.; Cheylyakh, D. Slag waste of metallurgical production. Environmental and economic justification of their use in industry in Ukraine. *Polityka Energetyczna Energy Policy J.* **2021**, *24*, 169–182. [CrossRef]
34. Galaburda, M.; Kovalska, E.; Hogan, B.T.; Baldycheva, A.; Nikolenko, A.; Dovbeshko, G.I.; Oranska, O.I.; Bogatyrov, V.M. Mechanochemical synthesis of carbon-stabilized Cu/C, Co/C and Ni/C nanocomposites with prolonged resistance to oxidation. *Sci. Rep.* **2019**, *9*, 17435. [CrossRef] [PubMed]
35. Galaburda, V.; Bogatyrov, V.M.; Skubiszewska-ZiŁba, J.; Oranska, O.I.; Sternik, D.; Gun'ko, V.M. Synthesis and structural features of resorcinol formaldehyde resin chars containing nickel nanoparticles. *Appl. Surf. Sci.* **2016**, *360*, 722–730. [CrossRef]
36. Galaburda, M.; Bogatyrov, V.; Sternik, D.; Oranska, O.; Borysenko, M.; ŠkorvÁnek, I.; Skwarek, E.; DeryŁo-Marczewska, A.; Gun'ko, V. Magneto-sensitive carbon-inorganic composites based on particleboard and plywood wastes. *Chem. J. Mold.* **2021**, *16*, 68–78. [CrossRef]

37. Gregg, S.J.; Sing, K.S.W. Adsorption, Surface Area and Porosity. In *Berichte der Bunsengesellschaft für Physikalische Chemie*, 2nd ed.; Auflage, Academic Press: London, UK, 1982; Volume 86, p. 957.
38. Gun'ko, V.M.; Mikhalovsky, S.V. Evaluation of slitlike porosity of carbon adsorbents. *Carbon* **2004**, *42*, 843–849. [[CrossRef](#)]
39. Neimark, A.V.; Ravikovitch, P.I.; Vishnyakov, A. Adsorption hysteresis in nanopores. *Phys. Rev. E* **2000**, *62*, R1493(R). [[CrossRef](#)]
40. Ravikovitch, P.I.; Domhnaill, S.Ó.; Neimark, A.V. Capillary hysteresis in nanopores: Theoretical and experimental studies of nitrogen adsorption on MCM-41. *Langmuir* **1995**, *11*, 4765–4772. [[CrossRef](#)]
41. Li, J.; Feng, Y.; Li, H.; Zhang, Q. Study of recycling blast furnace dust by magnetization roasting with straw charcoal as reductant. *Physicochem. Probl. Miner. Process.* **2022**, *58*, 149265. [[CrossRef](#)]
42. Ferrari, A.C. Raman spectroscopy of graphene and graphite: Disorder, electron–phonon coupling, doping and nonadiabatic effects. *Solid State Commun.* **2007**, *143*, 47–57. [[CrossRef](#)]
43. Galaburda, M.V.; Bogatyrov, V.M.; Borysenko, M.V.; Oranska, O.I.; Sternik, D.; Sidorenko Voitko, I.; Derylo-Marczewska, A. Magnetosensitive C/Fe adsorbents synthesized from lignin. In Proceedings of the Ukrainian Conference with International Participation “Chemistry, Physics and Technology of Surface” Dedicated to the 90th Birthday of Aleksey Chuiko, Academician of NAS of Ukraine, Kyiv, Ukraine, 21–22 October 2020. [[CrossRef](#)]
44. Wang, Y.; Alsmeyer, D.C.; McCreery, R.L. Raman spectroscopy of carbon materials: Structural basis of observed spectra. *Chem. Mater.* **1990**, *2*, 557–563. [[CrossRef](#)]
45. Gul, E.; Alrawashdeh, K.A.B.; Masek, O.; Skreiberg, O.; Corona, A.; Zampilli, M.; Wang, L.; Samaras, P.; Yang, Q.; Zhou, H.; et al. Production and use of biochar from lignin and lignin-rich residues (such as digestate and olive stones) for wastewater treatment. *J. Anal. Appl. Pyrolysis* **2021**, *158*, 105263. [[CrossRef](#)]
46. Szymański, G.S.; Karpinski, Z.; Biniak, S.; Swiatkowski, A. The effect of the gradual thermal decomposition of surface oxygen species on the chemical and catalytic properties of oxidized activated carbon. *Carbon* **2022**, *40*, 2627–2639. [[CrossRef](#)]
47. Derylo-Marczewska, A.; Mirosław, K.; Marczewski, A.W.; Sternik, D. Studies of adsorption equilibria and kinetics of o-, m-, p-nitro- and chlorophenols on microporous carbons from aqueous solutions. *Adsorption* **2010**, *16*, 359–375. [[CrossRef](#)]
48. Bogatyrov, V.M.; Borysenko, M.V.; Oranska, O.I.; Galaburda, M.V.; Makhno, S.M.; Gorbyk, P.P. Synthesis and properties of metal-carbon nanocomposites Ni/C, Co/C and Cu/C with high metal content. *Poverhn.* **2017**, *9*, 136–144. [[CrossRef](#)]
49. Azizian, S.; Eris, S.; Wilson, L.D. Re-evaluation of the century-old Langmuir isotherm for modeling adsorption phenomena in solution. *Chem. Phys.* **2018**, *513*, 99–104. [[CrossRef](#)]
50. Kujawska, J.; Wasag, H. Biochar: A low-cost adsorbent of Methylene Blue from aqueous solutions. *J. Phys. Conf. Ser.* **2021**, *1736*, 012002. [[CrossRef](#)]
51. Ouedrhiri, A.; Lghazi, Y.; Bahar, J.; Ait Himi, M.; El Haimer, C.; Youbi, B.; Khoukhi, M.; Bimaghra, Y. Adsorption of the Methylene Blue Dye in Environmental Water Samples by Biochar Obtained from the Valorization of Argan Shells. *Phys. Chem. Res.* **2022**, *10*, 301–313. [[CrossRef](#)]
52. Bordoloi, N.; Deep Dey, M.; Mukhopadhyay, R.; Katak, R. Adsorption of Methylene blue and Rhodamine B by using biochar derived from Pongamia glabra seed cover. *Water Sci. Technol.* **2018**, *77*, 638–646. [[CrossRef](#)] [[PubMed](#)]
53. Limaa, R.S.; Paiva e Silva Zanta, C.L.; Meilib, L.; Santos Lins, P.V. Souza dos Santos, G.E.; Tonholo, J. Fenton-based processes for the regeneration of biochar from Syagrus coronata biomass used as dye adsorbent. *Desalination Water Treat.* **2019**, *162*, 391–398. [[CrossRef](#)]
54. Sun, L.; Wan, S.; Luo, W. Biochars prepared from anaerobic digestion residue, palm bark, and eucalyptus for adsorption of cationic methylene blue dye: Characterization, equilibrium, and kinetic studies. *Bioresour. Technol.* **2013**, *140*, 406–413. [[CrossRef](#)]
55. Lesbani, A.; Asri, F.; Palapa, N.R.; Taher, T.; Rachmat, A. Efficient Removal of Methylene Blue by Adsorption Using Composite Based Ca/Al Layered Double Hydroxide-Biochar. *Glob. Nest J.* **2020**, *22*, 250–257. [[CrossRef](#)]
56. Sáenz-Alanís, C.A.; García-Reyes, R.B.; Soto-Regalado, E.; García-González, A. Phenol and methylene blue adsorption on heat-treated activated carbon: Characterization, kinetics, and equilibrium studies. *Adsorpt. Sci. Technol.* **2017**, *35*, 789–805. [[CrossRef](#)]
57. Kannan, N.; Sundaram, M. Kinetics and mechanism of removal of methylene blue by adsorption on various carbons—A comparative study. *Dyes Pigments* **2001**, *51*, 25–40. [[CrossRef](#)]

**Disclaimer/Publisher's Note:** The statements, opinions and data contained in all publications are solely those of the individual author(s) and contributor(s) and not of MDPI and/or the editor(s). MDPI and/or the editor(s) disclaim responsibility for any injury to people or property resulting from any ideas, methods, instructions or products referred to in the content.